The fluctuation-dissipation measurement instrument at the Linac Coherent Light Source

Cite as: Rev. Sci. Instrum. 93, 083902 (2022); https://doi.org/10.1063/5.0091297 Submitted: 14 March 2022 • Accepted: 30 June 2022 • Published Online: 10 August 2022

T. A. Assefa, D M. H. Seaberg, D A. H. Reid, et al.







ARTICLES YOU MAY BE INTERESTED IN

Skyrmion fluctuations at a first-order phase transition boundary
Applied Physics Letters 116, 181901 (2020); https://doi.org/10.1063/5.0004879

High frequency properties of a planar ion trap fabricated on a chip Review of Scientific Instruments 93, 083202 (2022); https://doi.org/10.1063/5.0091745

Thin head atomic force microscope for integration with optical microscope
Review of Scientific Instruments 93, 083702 (2022); https://doi.org/10.1063/5.0093080





The fluctuation-dissipation measurement instrument at the Linac Coherent Light Source

Cite as: Rev. Sci. Instrum. 93, 083902 (2022); doi: 10.1063/5.0091297 Submitted: 14 March 2022 • Accepted: 30 June 2022 •







Published Online: 10 August 2022

T. A. Assefa,^{1,2} M. H. Seaberg,³ D A. H. Reid,³ L. Shen,^{1,2} V. Esposito,¹ G. L. Dakovski,³ W. Schlotter,³

B. Holladay,^{3,4} R. Streubel,^{5,6} D S. A. Montoya,⁷ P. Hart,³ D K. Nakahara,³ S. Moeller,³ D S. D. Kevan,^{8,9} D P. Fischer,⁵ E. E. Fullerton,^{7,10} W. Colocho,³ D A. Lutman,³ D F.-J. Decker,³ D S. K. Sinha,⁴ S. Roy,⁹

E. Blackburn,² and J. J. Turner^{1,3,a)}

AFFILIATIONS

- ¹Stanford Institute for Materials and Energy Science, Stanford University and SLAC National Accelerator Laboratory, Menlo Park, California 94025, USA
- ²Division of Synchrotron Radiation Research, Department of Physics, Lund University, 22100 Lund, Sweden
- ³Linac Coherent Light Source, SLAC National Accelerator Laboratory, Menlo Park, California 94720, USA
- Department of Physics, University of California—San Diego, La Jolla, California 92093, USA
- ⁵Materials Sciences Division, Lawrence Berkeley National Laboratory, Berkeley, California 94720, USA and Physics Department, University of California Santa Cruz, Santa Cruz, California 95064, USA
- ⁶Department of Physics and Astronomy and Nebraska Center for Materials and Nanoscience, University of Nebraska-Lincoln, Lincoln, Nebraska 68588, USA
- Center for Memory and Recording Research, University of California—San Diego, La Jolla, California 92093, USA
- ⁸Department of Physics, University of Oregon, Eugene, Oregon 97401, USA
- 9Advanced Light Source, Lawrence Berkeley National Laboratory, Berkeley, California 94720, USA
- ¹⁰ Department of Electrical and Computer Engineering, University of California—San Diego, La Jolla, California 92093, USA

ABSTRACT

The development of new modes at x-ray free electron lasers has inspired novel methods for studying fluctuations at different energies and timescales. For closely spaced x-ray pulses that can be varied on ultrafast time scales, we have constructed a pair of advanced instruments to conduct studies targeting quantum materials. We first describe a prototype instrument built to test the proof-of-principle of resonant magnetic scattering using ultrafast pulse pairs. This is followed by a description of a new endstation, the so-called fluctuation–dissipation measurement instrument, which was used to carry out studies with a fast area detector. In addition, we describe various types of diagnostics for single-shot contrast measurements, which can be used to normalize data on a pulse-by-pulse basis and calibrate pulse amplitude ratios, both of which are important for the study of fluctuations in materials. Furthermore, we present some new results using the instrument that demonstrates access to higher momentum resolution.

Published under an exclusive license by AIP Publishing. https://doi.org/10.1063/5.0091297

I. INTRODUCTION

The fluctuation–dissipation theorem describes a general relationship between the response of a system to an external field and the internal fluctuations of the system in the absence of the field at thermal equilibrium. These fluctuations are characterized by a correlation function of relevant physical quantities of the system fluctuating in thermal equilibrium, also known as the fluctuation

spectra. This theorem provides a way to measure the microscopic interactions responsible for short-ranged ordering through these spectra if fluctuations can be measured in equilibrium.

While understanding ground state fluctuations is fundamental to comprehending the underlying physics of a system, it is considerably more challenging in quantum materials. This is especially true of states that are electronic in origin and that depend on strong electron correlations, both from an experimental as well as a

a) Author to whom correspondence should be addressed: joshuat@slac.stanford.edu

theoretical perspective, because the Hamiltonian cannot be represented with a small-valued, perturbative parameter. For instance, in a magnetic system, the observation of the spin fluctuation spectrum can be related back to the microscopic interactions and even shed light on the macroscopic properties of the material as well. For instance, in the quantum critical region, the system can be viewed as a perfect fluid, and the system will exhibit a relaxation time given purely by quantum mechanics, $\tau = \frac{\hbar}{k_B T}$. Outside of this region, however, the fluctuation time will slow and can depend on other energies, such as the exchange interaction of the Hamiltonian (see Fig. 1). Fluctuation measurements then provide a direct method of measuring microscopic interactions.

X-ray photon correlation spectroscopy (XPCS) is a primary technique to study fluctuations in materials, made possible by the construction of high-brightness synchrotron radiation sources. XPCS and other related methods allow for studying both dynamics and memory effects. For example, coherent radiation can be used to compare domain structure for different control parameters, such as magnetic thin films, 3,4 cuprate superconductors, 5 and stripe ordered nickelates.6 In the realm of temporal fluctuations, since the first XPCS experiments performed almost 30 years ago7 using coherent x rays,8 the field has made remarkable success in looking into slow fluctuations in alloys, thin films, colloidal systems, and antiferromagnets. 9-13 Resonant x-ray scattering has also made an impact due to the ability to resonantly tune to important elements and directly study order parameters, such as insulators exhibiting spiral antiferromagnets, 16 charge order, 17 and orbital ordering,¹ thermally driven spin-reorientation transitions.¹⁸ This is especially

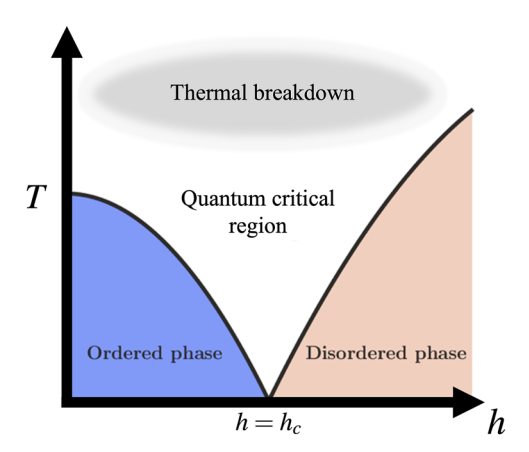


FIG. 1. A schematic demonstrating the quantum critical region, based on studies from Sachdev and Ye. ¹⁹ The phase diagram shows temperature vs a control parameter, h, such as pressure or magnetic field. The blue represents the ordered phase outside of which thermal fluctuations cause the destruction of the ordered phase. The orange region is quantum disordered, where no long range order is detected, and a region where excitations can, like the ordered phase, be described quasi-classically. The central, white region represents regions of the phase diagram heavily influenced by the quantum critical point found at $h = h_c$. Here, the fluctuations can display nontrivial, strongly coupled dynamics or entangled excitations and can occur on fast timescales, bound to a minimum speed of $\tau = \hbar (k_B T)^{-1}$. At some higher temperature cutoff, the fluctuations will depend on the specifics of the problem, such as the exchange interaction between spins on the lattice.

critical in the soft x-ray regime, where the x-ray energy resonances occur for important elements, and remarkable success has occurred for the study of electronic and magnetic phenomena.

However, the shortest timescales that can be probed with even the best x-ray sources are still limited by the available coherent flux and the detector readout rate. The advent of fourth-generation x-ray free-electron laser (XFEL) sources based on self-amplified spontaneous emission (SASE) provides spatially coherent and ultrashort pulses with extremely high peak-brightness and points to the detector development as the highest priority. Even with the best stateof-the-art detectors that have come over the years with improved dynamic range and the detector readout rate, 20-24 the shortest timescales that can be achieved is at the level of the microsecond timescale, although recent work has reported 192 ns pulse separation using the intrinsic bunch structure the storage ring at PETRA III.²⁵ For this reason, access to dynamics in materials at faster timescales is being carried out by implementing approaches at pulsed XFEL sources that add x-ray pulses, 26 and the time dependence of the fluctuations at the level of this time separation time can be recovered by studying the distribution of the photon fluctuations, which we refer to from this point as x-ray Photon Fluctuation Spectroscopy (XPFS).²⁷ This is typically carried out using split-and-delay optical setups^{28–31} and two-bucket modes, ^{32–37} which can span the picoseconds and nanoseconds timescales, respectively. This opens a new avenue to probe ultrafast dynamics in materials, yet the instrumentation has been lacking to take full advantage of this goal based on these XFEL developments, especially as applied to resonant coherent scattering, which can be important in the field of quantum materials discussed above.

At the Linac Coherent Light Source (LCLS), we have developed a new instrument, the fluctuation-dissipation measurement (FDM) machine, to achieve this goal. We demonstrate its utility by investigating spontaneous fluctuations through the illumination of a material system with ultrashort pairs of x-ray pulses generated in the electron accelerator. ^{38–42} The construction of this instrument was shown to be capable of capturing about 1500 times more information per single x-ray shot to understand the skyrmion physics through the fluctuation spectrum. This was made possible by designing an instrument with a larger high-speed detector, an ability to place it farther from the sample, and the option to produce larger speckle sizes. Taken together, this provides the potential to measure ~1200 times more speckle coherence areas at the detector plane and the ability to access a solid angle of about ~1500 times larger than the prototype instrument. We used it to probe not only the pure skyrmion lattice³⁵ but also the mixed skyrmionstripe state,³⁴ where the new setup could measure the full skyrmion speckle diffraction pattern in a single shot. We found evidence of both highly dynamic skyrmion fluctuations that slow down at the critical point in the former³⁵ as well as slower jamming behavior near the boundary of the skyrmion lattice phase in the latter phase.³⁴ This technique allows one to probe dynamics from hundreds of picoseconds to several nanoseconds range,²⁷ and it is equally possible to use the technique in a wide-angle diffraction geometry to investigate electronic order fluctuations in strongly correlated quantum materials.

In this article, we report the comprehensive progression of instrumentation advancement by first discussing a prototype instrument, followed by a more sophisticated apparatus that can capture substantially more data per shot. We describe the pair of instruments in detail, followed by two different types of novel diagnostics that were developed for this effort. Finally, we present original data on a skyrmion lattice of the correlation function measured at the second-order skyrmion lattice peak. This high momentum scattering is made possible with the enhanced instrumentation discussed here, enabling data collection using a large-area detector placed far from the sample in an ultra-high vacuum environment to formulate ultrafast coherent soft x-ray speckle.

II. INSTRUMENTS

X-ray Photon Fluctuation Spectroscopy (XPFS) experiments were carried out by constructing a prototype instrument for conducting a proof-of-principle study. This was followed by a new instrument specifically designed to study topological chiral magnetic fluctuations in a thin film. We describe both of these instruments below in Secs. II A and II B, respectively.

A. The XPFS prototype instrument

The first XPFS prototype instrument consists of a sample manipulator and in-house built electro-magnet enclosed in a UHV sample chamber, a guard aperture, and an Andor (Newton SO) CCD detector mounted in transmission geometry. This provided direct x-ray detection, high efficiency, single photon sensitivity, and 2D imaging at 120 Hz. The detector was mounted on a translation motion that added the ability to change the sample to detector distance, allowing for the tuning of the optimum speckle size on the detector. By masking a portion of the chip from detecting any x-ray photons, these commercially available "slow" detectors can run at higher repetition rates. We tested a number of different configurations, where smaller active areas can be read out at higher speeds (see Appendix A). We chose to run the soft x-ray detector in a read-out mode to collect data at 120 Hz, the maximum repetition rate of the LCLS at the time of measurement, by reducing the data collection array to 90×90 pixels. This only gives reliable results if the active area is the only region being illuminated with photons. We built a remote motorized mask on a two-dimensional stage to move in the two orthogonal directions to the beam. This masking device was used to block x-ray illumination to the rest of the CCD chip while collecting data over the small region of interest, allowing us to increase the data readout rates. Results from the first use of this instrument were published in Seaberg et al.32

One diagnostic tool, which is critical for operation in this mode, is a pulse-sorting amplitude detector. For this, we used a Hamamatsu microchannel plate (MCP) detector, which is typically used as an I_0 monitor for the incoming intensity after the monochromator. This consisted of an annulus model, where the incoming beam travels through the hole in the center and strikes a transparent membrane, such as SiN_4 , which is inserted into the beamline directly after the detector. The absorbed signal is re-radiated from the membrane into the MCP and ran through a home-built, AC de-coupling box and then into a fast digitizer. At nanosecond time delays, a high-frequency digitizer with a 3 GHz bandwidth and an 8 GS/s sampling rate is fast enough to resolve the pulse height of each individual pulse for pulse sorting. This is typically processed through

singular value decomposition (SVD) pulse analysis, as discussed in Sec. $\overline{\text{III B}}$.

The main motivation for this diagnostic is not to monitor the incoming flux but to record the relative amplitude of each pulse within the pulse pair. As the amplitude fluctuations can be substantial due to the SASE process and because the beam travels through a narrow band monochromator, 43 this information is critical for the measurement. A typical speckle pattern generated from the pulse pair using the prototype instrument was about 100-1000 total photons (see Fig. 2 for an example). Given that the photons illuminating the sample numbered about 10¹⁰ per pulse, it is clear that significant sensitivity is needed. In order to achieve a reasonable signal to noise ratio per data point, we have to acquire about 100 000 images, almost 15 min of continuous data collection at 120 Hz. In XPFS, however, the overall incoming intensity is important not only for signal to noise considerations but also must be low enough to not produce unwanted excitations in the system. To address this, additional attenuation was used, such as solid filters, but was placed after this monitor to ensure that enough signals were present to illuminate the MCP for high performance, enable appropriate amplitude sorting, and also set the proper x-ray fluence on the sample. In the case above, aluminum filters with a thickness of \sim 24 μ m were used to attenuate about 91% of the beam at this wavelength.

Finally, the above instrumentation advancements as well as the FDM machine described in Sec. II B were all developed for integration at the soft x-ray materials instrument 44 at the Linac Coherent Light Source. This instrument consists of timing tool diagnostics, $^{46-48}$ a varied line space monochromator, and a Kirpatrick–Baez mirror system. The latter is a pair of orthogonal cylindrical mirrors coated with B₄C to reduce heat load, which can bend the mirror surface elliptically to create an x-ray focal spot between 1 mm and a couple of microns at the sample position. This system images the source horizontally and the monochromator exit slit vertically and uses a gas monitor detector to characterize the x-ray transmission with wavelength. A number of endstations

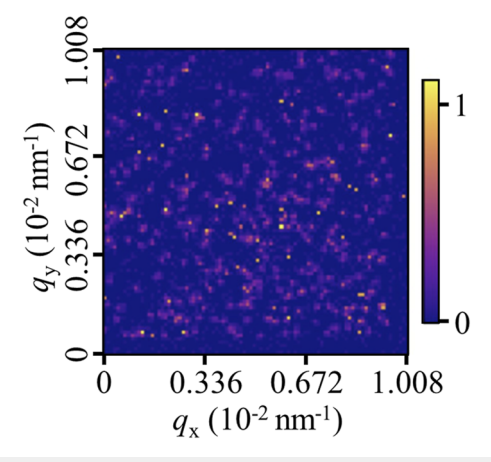


FIG. 2. A single shot speckle pattern for data collected with the XPFS prototype instrument. The region of the detector used was 90×90 pixels, the largest area to readout for the repetition rate of 120 Hz using the fastest ADC speed (see Appendix A). The units are converted to single photon events for this image.

have been integrated to make use of this soft x-ray system. ^{55–59} More information can be found in the work by Schlotter *et al.* ⁶⁰ on the details of this system. A next generation soft x-ray beamline is currently under commissioning at the LCLS-II, and the integration of this XPFS prototype instrument was used for recent experiments at this beamline. This development will be described in a forthcoming article.

B. Fluctuation-dissipation instrument

For the latest XPFS experiments, we have constructed a new portable instrument that was also coupled to the soft x-ray research (SXR) beamline (shown in Fig. 3). The purpose of this instrument design, the fluctuation–dissipation measurement (FDM) machine, was two-fold: to capture the full diffraction pattern instead of a limited region of interest at the magnetic skyrmion peak that was provided with the XPFS prototype instrument, and to increase the signal.

The first goal was carried out by designing a chamber centered around a large megapixel area detector that can be read out at the full 120 Hz repetition rate of the LCLS, although this would also be adaptable to future high-repetition rate detectors as well. The detector used here is a custom-designed system built around a pn-junction CCD sensor developed at the Halbleiterlabor (HLL, Germany) and is an imaging detector consisting of an array of 1024×1024 pixels of 75 μ m pitch with single photon sensitivity. The camera has two half-plane sensors that can be moved independently to maximize angular acceptance and was previously used in another instrument at the LCLS known as the LAMP.⁶¹ Notches allow the beam to pass when there is no gap between the sensors. The detector was gain- and energy-calibrated during the experiment. See Strüder et al. for more details on the detector.⁶²

The second goal was to increase the signal, but this cannot simply be achieved by increasing the photon flux on the sample, since we must work in the perturbative regime for XPFS.³² For a given repetition rate, by increasing the spot size on the sample, one can increase the pulse energy on the sample while keeping the incident fluence below the desired threshold. This is coupled with an upper limit constraint on the spot size to keep in mind for designing XPFS experiments, which is based on the average speckle size. This is more generally a volume in reciprocal space and has been computed previously, ^{63,64} but this can be approximated in two dimensions for a forward scattering geometry by the diameter of the speckle *s*, given by

$$s = \frac{z\lambda}{2\pi R},\tag{1}$$

where z is the sample to detector distance, λ is the wavelength of the radiation, and R is the diameter of the x-ray spot size on the sample. The factor of 2π comes from the fact that we usually use the elliptical mirror system to focus the beam (Sec. II A), which serves to define the coherence length at the sample, since the beam is nearly fully coherent. Equation (1) assumes a Gaussian intensity distribution at the focal point, which has been shown to be a good approximation in x-ray ablation studies of high-Z elements performed at the LCLS. So,51

To maximize the available signal impinging on the sample, we expand the x-ray spot size as much as possible while holding to the constraints governed by Eq. (1), which requires the detector to be

placed as far as possible from the sample. Since the SXR hutch is 10 m, and the distance from the vertical, second Kirkpatrick-Baez (KB) mirror to the back wall is 4.8 m, we designed the endstation to optimize the entire space between the nominal focal position and the back wall of the SXR experimental hutch, 60 making the final instrument length 3.454 m with a spot size of about 30 $\mu \rm m$. The maximum sample-to-detector distance z was measured to be 2.35 m as a result of this design. With the addition of the large area detector and the increased distance of it to the sample, this new instrument has the ability to capture about 1500 times more information per x-ray pulse pair than the XPFS prototype instrument described in Sec. II A.

To mount a heavy detector at such a large distance from the sample chamber under UHV conditions, we installed a second chamber to support the detector and connected it with a large 5 in. diameter stainless steel drift tube. This secondary chamber was also used to support additional pumping for the detector, two 700 l/s turbo pumps, to keep the detector in an ultraclean state. Both vacuum systems had independent motor control and were connected through UHV edge-welded bellows. The first results using this instrument were published in Esposito *et al.*³⁴ and in Seaberg *et al.*³⁵

III. DIAGNOSTICS

For completeness, we discuss two important diagnostics we have developed below which are important for successful XPFS experiments. This is an *in situ* monitor, which captures the contrast measurement from the sample for each shot of the measurement and acts as a diagnostic on the x-ray pulse properties. The second device records the pulse amplitude for each pulse. This can both serve as a real-time monitor for tuning the beam properties during a measurement as well as allow for a grouping of the data based on the pulse amplitude ratio for finer contrast analysis. We discuss methods for analyzing these pulse amplitudes further in Appendix B.

A. Contrast monitor

An additional diagnostic included in the FDM instrument was what we call a "contrast monitor." The purpose of this was to monitor the contrast from an independent sample in situ on a shot-by-shot basis to remove any ambiguities from sources, such as machine parameter changes, transverse coherence fluctuations, or other undesired experimental subtleties. We tested multiple versions of this new tool, and it consisted of a thin membrane sprinkled with micro-sized porous glass or gold particles that had been characterized previously by coherent x rays.⁶⁶ By inserting this into the chamber together with the magnetic sample, scattering from the glass could be monitored continuously to understand if the beam properties were changing during the experiment. The glass particle size was chosen to be about ~500 nm such that the maximum momentum transfer vector from the nanoparticle distribution q_{σ} was less than the skyrmion momentum, making it possible to be measured simultaneously during the experiment, i.e., $q = 0 < q_o$ $< q_s$, as shown in Fig. 4(a). The inner bright disk of small-angle scattering is due to the glass structure, which was mounted behind the poles of a custom-built electromagnet due to the small space constraints within the electromagnet itself. The outer ring, two bright peaks together with four weaker peaks at the same radius from q = 0, shows the skyrmion lattice scattering,⁶⁷ which scatters to the

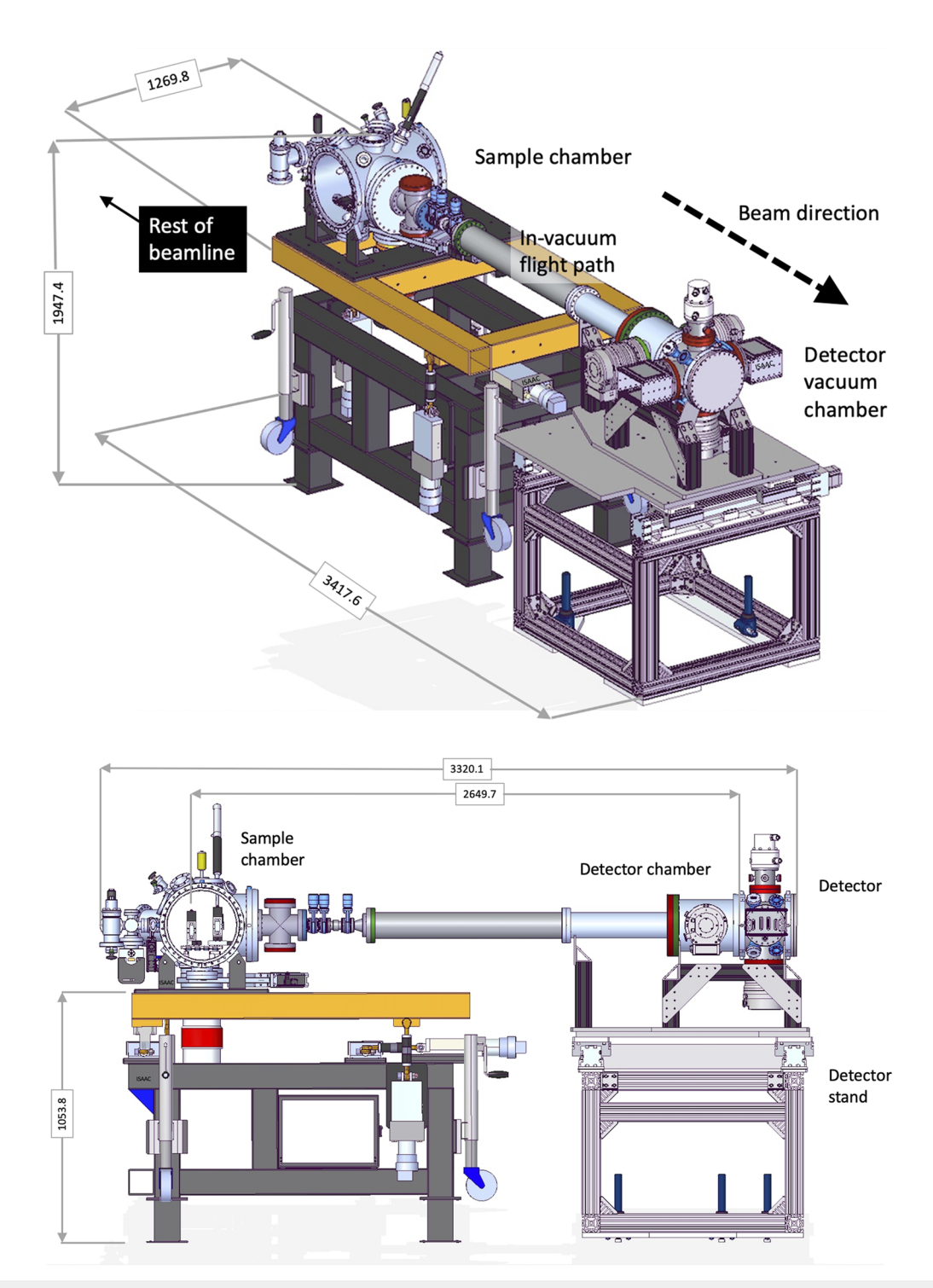


FIG. 3. The Fluctuation–Dissipation Measurement (FDM) machine. The instrument design was engineered for the purposes of carrying out XPFS in a forward scattering geometry at the soft x-ray branchline 4d of the LCLS. 45 It includes two different UHV chambers, each with its own support stand. The first houses the sample environment (left side), including an electromagnet, sample manipulator, spot size and timing diagnostics, as well as a contrast monitor. The second chamber (right side) was built to house the pnCCD detector, a one megapixel detector that runs at 120 Hz, although future detectors can be adapted as well. The adjoining components were designed to maximize the distance of the sample to the detector as well as to include additional diagnostics to insert into the beam between the sample environment and the detector. The orientation of the bottom view shows the sample chamber (left), detailing the sample and field motion, different sets of filers on the adjoining drift tube (middle), and the detector vacuum chamber (right). All dimensions are given in mm.

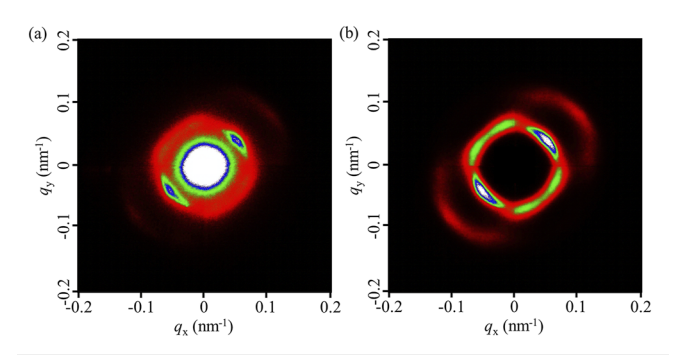


FIG. 4. The contrast monitor. (a) The combined scattering pattern of the nanoporous glass particle scattering, shown as the bright disk around the q=0 position, acts as the contrast monitor, together with the higher-q scattering of the skyrmion lattice. (b) The skyrmion lattice scattering pattern collected after the removal of the contrast monitor.

higher q, designated as q_s . For comparison, Fig. 4(b) shows the skyrmion lattice without the contrast monitor.

When the speckle size is comparable to or smaller than the detector pixel size, the effective contrast can artificially decrease. For instance, Sandy *et al.*⁶⁸ showed that the contrast $\tilde{C}(q,t)$ should be multiplied by a multiplicative factor to take this into account,

$$C(q,t) = \tilde{C}(q,t) \frac{\Delta_r}{\sqrt{\Delta_r^2 + \Delta_d^2}},$$
 (2)

where we have adopted their notation for speckle width in cylindrical coordinates Δ_r and detector pixel width Δ_d and where the reduction in contrast due to the speckle width in the z-direction is negligible.⁶³ As a result, by starting with full speckle contrast, one can take Eq. (2) and use the contrast monitor to indirectly measure the speckle size and hence the approximate beam size at the sample. This diagnostic can additionally be used as a method to indirectly measure the focus while adjusting it with the KB mirror system by translating the focal point through the sample position. An example of a focal scan using the contrast monitor is shown in Fig. 5. Similar ideas have also been proposed with transmissive gratings.⁶⁹ Recent developments have furthermore been exploring the use of single-shot wavefront sensors to characterize the distribution of both the intensity and local electric field at the sample plane.⁷⁰ These are based on Talbot interferometry and are very robust and sensitive, but they cannot be used in parallel with a transmission geometry experiment such as that demonstrated

B. Two-pulse amplitude detection

In order to reliably extract the contrast of the summed speckle pattern, it is crucial to determine the ratio of the incoming pulse intensities within each pulse pair. This is particularly challenging for sub-nanosecond timescales. We achieved this by fabricating a device to handle sensitivity to soft x rays and using a microchannel plate (MCP) to measure the fluorescence from a transparent SiN_x membrane placed in the beam. A custom-built aluminum paddle was designed to insert into the beam path with multiple window

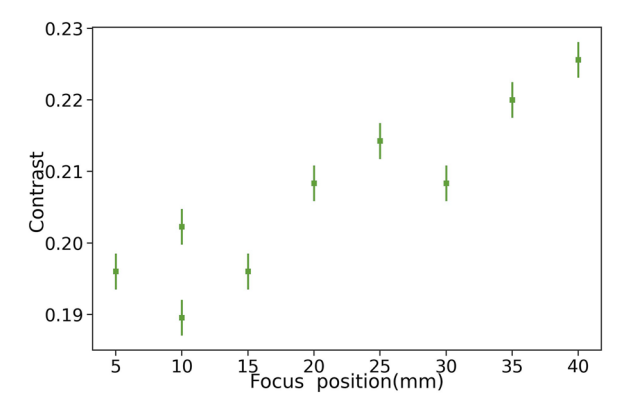


FIG. 5. Focal contrast scan. Using the contrast monitor fabricated with nanoporous glass, we observed a roughly linear trend in contrast as a function of focal position, indicating that the contrast was artificially reduced due to under-sampling of the speckle pattern for the position of the monitor. Assuming maximum contrast, the speckle size and hence the approximate beam size at the sample can be estimated. This corresponds to a 55–65 μ m spot size at the sample, which is consistent with the YAG-based microscope measurement we observed of $\approx\!50~\mu$ m FWHM.

positions and offer different thickness membranes to optimize the transmission of the x rays and strength of the scattered signal. However, the digitized waveforms present a multi-peak structure with long-lived effects, such as ringing. These effects often overlap when measuring two pulses, especially at shorter delays. Consequently, a simple integration of the peak intensity does not provide a reliable measurement. There are three sources of variance in the arrival of the waveforms. The overall timing jitter of the bunch (70 fs rms) and the difference in timing of each electron bunch within the pair, which depends on the separation distance between each pulse (20 fs rms, for a pulse separation of 200 ns), are each fairly small, but each is swamped by the trigger jitter in this mode (265 ps rms). To handle this, an approach based on singular value decomposition (SVD) is well suited here.

First, an orthonormal single-pulse basis is constructed based on a set of single-pulse reference waveforms using SVD. The single pulse waveforms are stacked in a matrix A, and its SVD is computed via

$$A = U\Sigma V^*, \tag{3}$$

with Σ being a diagonal matrix containing the eigenvalues and U and V being unitary matrices. The columns of the matrix V form an orthonormal basis of the row space of A and can be used to reconstruct the reference waveforms. By creating an appropriate basis, this approach allows for an approximation of the waveforms using only a few coefficients. In fact, the component with the largest eigenvalue often already largely reproduces the main features of the waveform. The second coefficient is related to the first derivative and captures shifts in the timing of the amplitude pulse that was mentioned earlier. In the top panel of Fig. 6, an example dataset of a single-pulse waveform is shown together with the first three components from the SVD using 500 waveforms. Here, it is clear that the third

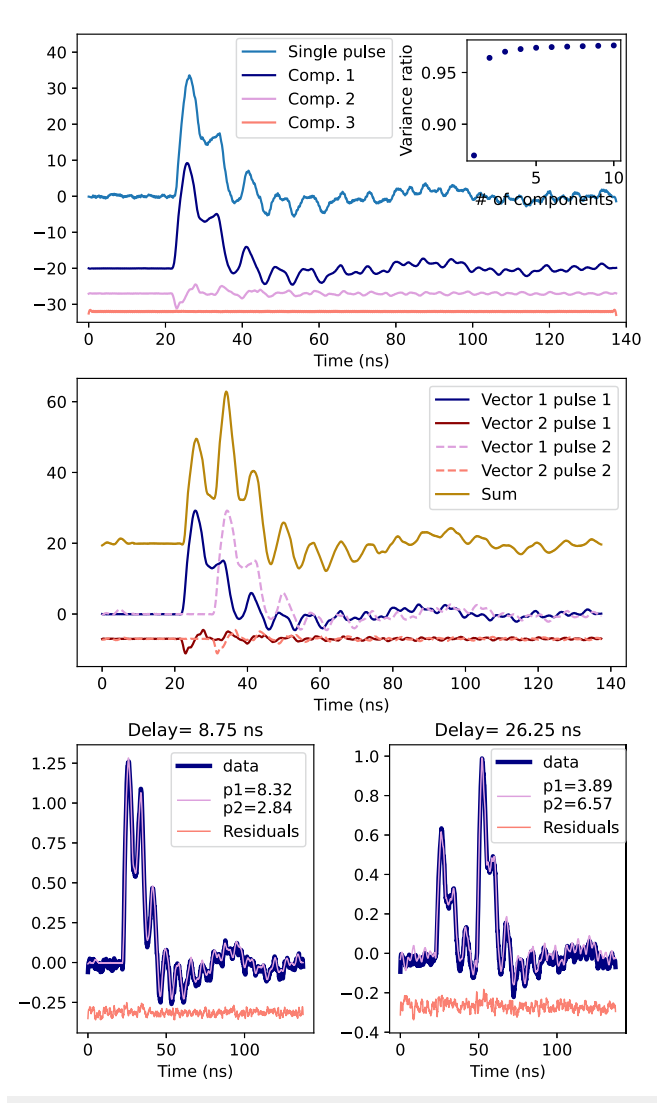


FIG. 6. Singular value decomposition analysis of the double pulse waveforms. Top: A single pulse waveform as measured by an MCP and the first three components from the SVD on 500 such waveforms, offset for clarity. In order to highlight the importance of each component, each vector is multiplied by its corresponding eigenvalue. The SVD components are offset vertically for the sake of clarity. The inset shows the ratio of explained variance as a function of the number of components. Middle: Construction of the double pulse basis achieved by shifting two single pulse basis vectors with respect to each other to match the time delay between them. The different sets of curves are offset vertically for clarity. Bottom: Examples of reconstructed waveforms for two different time delays showing both the data and the reconstructed SVD waveforms. The intensity of each individual pulse is indicated in the legend. The residual of the reconstructions is near zero but offset here for clarity, demonstrating how well this method performs for extracting the amplitudes of each pulse.

component contains fairly small corrections. A good way to quantify this is the amount of explained data variance as successive components are added to describe the data. As shown in the inset of Fig. 6, the explained variance ratio increases dramatically for the first few components, passing the 95% mark for the second component. The

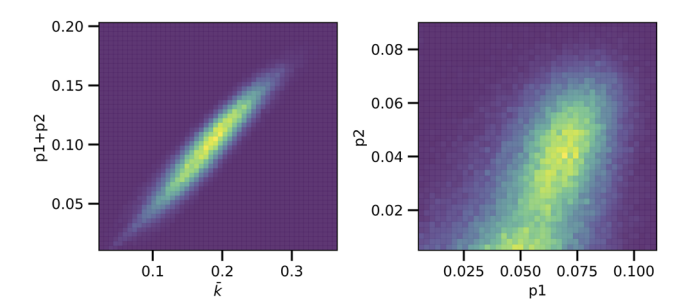


FIG. 7. Correlation histograms of the reconstructed intensities for about 140 000 shots at the LCLS free-electron laser. Left: sum of the reconstructed intensity $p_1 + p_2$ as a function of the average intensity on the detector \bar{k} . Right: correlation between the two pulses, p_1 and p_2 .

shot-to-shot variation of the pulse intensity can thus be accounted for by only a small number of eigenwaveforms.

Using the selected components, a two-pulse basis W is then constructed by shifting one single pulse basis set to the position of the second pulse. The two-pulse basis vectors are shown in the middle panel of Fig. 6. Two components are used for each pulse here, shifted with respect to each other by the known delay between the pulses, 8.75 ns in this case. However, it should be noted here that the basis is then no longer orthonormal (see Appendix B for more details). The sum of all basis vectors is shown in the top curve.

Examples of two different delays are shown at the bottom of Fig. 6. In the first case, with a delay of 8.75 ns, the two pulses are indistinguishable. To demonstrate the validity of the pulse amplitude identification procedure, we plot the residual of the reconstructed waveforms below the curves. These verify the quality of the reconstruction procedure and give confidence in using this to sort the amplitude ratios.

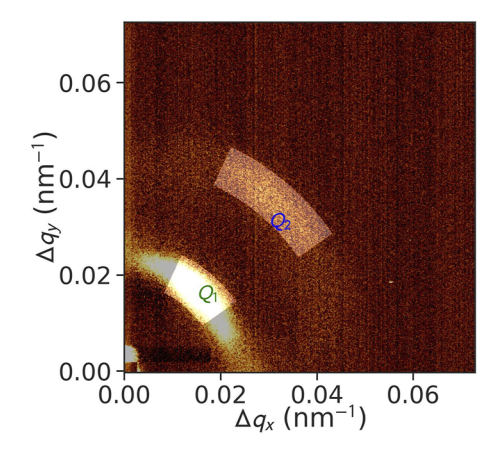
To validate this procedure, results from 140 000 two-pulse shots measured at the LCLS are summarized in Fig. 7. The summed pulse amplitude correlates linearly with the scattered intensity measured on a CCD soft x-ray detector. The second histogram on the right shows the correlation between the first and the second pulses. On average, the intensity of the first pulse was often higher than that of the second pulse for this dataset.

IV. RESULTS

To demonstrate the advantage of this instrument, we evaluated original data that had never been analyzed previously for a magnetic skyrmion system. Magnetic skyrmions are vortex-like spin-swirling structures that are topologically protected⁷¹ with a typical dimension of a few tens to one hundred nanometers, ⁷² formed in the presence of an applied magnetic field. Under particular conditions, skyrmions form stable spin textures with long-range ordering, a skyrmion lattice. Understanding the temperature- and magnetic-field dependency of the skyrmion lattice structure can play a significant role in advancing the fundamental understanding of topological spin solitons and in achieving the technological potential of novel spintronics.⁷³ Primarily, identifying and characterizing magnetic skyrmion lattices have occurred using small-angle neutron scattering, which can detect magnetic lattice parameters in the

range of 0.5–300 nm.^{74–76} Equally, Lorentz transmission electron microscopy^{71,72} and spin-resolved scanning tunneling microscopy⁷⁷ have further established the existence of these phases in different magnetic systems. X rays have also played an important role by tuning to the resonance of the magnetic atom to directly probe the skyrmion structure as well. ^{67,78–80} Although we previously reported the first results using this instrument on both a damped oscillation and a slow down observed in the time correlation function of the skyrmion lattice, ³⁵ with further development of XPFS using ultrashort x-ray pulses, we are poised to make additional contributions using x rays by measuring the spin fluctuation spectrum on nanosecond timescales using the FDM described here.

Measurement of the time correlation of the first-order peak in a mixed phase state was also carried out between the ferromagnetic stripe domains and the skyrmion lattice phase.³⁴ With the FDM instrument, we illustrate here that we can capture the second-order scattering from this magnetic system. This higher



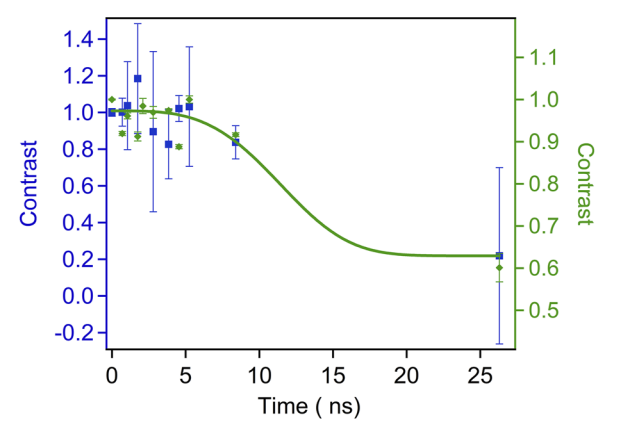


FIG. 8. (Top panel) One quarter of the pnCCD detector image measured from a FeGd sample in the stripe-skyrmion phase. The regions of interest (ROI) displayed in the image are used for the data shown in the right panel of the figure, with colors designating the two different peaks. (Bottom panel) Normalized two-pulse contrast from the first order peak (green diamonds) reported in Esposito *et al.*³⁴ and second order peak (blue squares) reported here from the same data collected in the stripe-skyrmion mixed phase. The fit shows compressed exponential dynamics with an exponent of 3.5, which shows quite different behavior from the exponential decay reported in the middle of the skyrmion phase.³⁵

order scattering, when strong enough to analyze, provides higher *q*-resolution data—something which will become important as XFELs move toward a high repetition rate. We use a similar procedure as reported previously³⁶ to analyze the data here, in search of fluctuations in the stripe-skyrmion mixed phase. Here, a photon map was produced from the photon.det code developed at LCLS,⁸¹ and single photon counting was used to extract the contrast.

We report the results in Fig. 8, which shows the time correlation function of the second-order peak in the skyrmion lattice system. For comparison, this is shown with the first order peak results and follows a similar dynamics, but with larger error bars due to the weaker intensity. The compressed exponential fit to the new data shows a larger drop compared to the first order peak, in addition to the larger error bar. Although studying higher order peaks with soft x rays will need high-repetition to become effective, it gives a higher momentum resolution and will be more sensitive to structural changes. With the higher repetition rate of LCLS-II on the horizon, for instance, we will be able to use an instrument such as the FDM to record data for experiments in a much shorter data collection time, about 10 000 times faster.

V. CONCLUSION

We describe the design and detail the operation of the fluctuation–dissipation measurement (FDM) instrument, which allows for the study of spontaneous fluctuations in magnetic or electronically ordered materials. We first describe a prototype instrument, which preceded the FDM instrument although it is still in use for special cases, before outlining the latest machine. The FDM was specifically designed for these types of measurements and is capable of capturing about 1500 times more information than its predecessor. In addition, we describe diagnostics developed as part of this work and show new results that are only made possible by the new capabilities offered by this innovation.

ACKNOWLEDGMENTS

The authors are grateful to Joseph Goodman for helpful discussions. Special thanks to Rick Bonnell for design work, Michael Holmes for engineering work, and Jeff Aldrich for construction and assembly work. This work was supported by the U.S. Department of Energy, Office of Science, Basic Energy Sciences, Materials Sciences and Engineering Division, under Contract No. DE-AC02-76SF00515. T.A.A., L.S., and E.B. acknowledge support from Lund University. The use of the Linac Coherent Light Source (LCLS), SLAC National Accelerator Laboratory, is also supported by the DOE, Office of Science under Contract No. DE-AC02-76SF00515. S.A.M. acknowledges support by the U.S. Office of Naval Research, In-House Lab Independent Research program. Portions of this work were supported by the U.S. Department of Energy, Office of Science, Basic Energy Sciences under Award No. DE-SC0022216. R.S., S.K.S., P.F., and S.R. acknowledge support from the U.S. Department of Energy, Office of Science, Office of Basic Energy Sciences, Materials Sciences and Engineering Division under Contract No. DE-AC02-05-CH11231 (NEMM program MSMAG). The research at UCSD was supported by the research programs of the U.S. Department of Energy (DOE), Office of Basic Energy Sciences (Award No. DE-SC0003678). J.J.T. acknowledges support from the U.S. DOE, Office of Science, Basic Energy Sciences through the

Early Career Research Program. R.S. acknowledges support from the National Science Foundation/EPSCoR RII Track-1: Emergent Quantum Materials and Technologies (EQUATE) under Grant No. OIA-2044049.

AUTHOR DECLARATIONS

Conflict of Interest

The authors have no conflicts to disclose.

Author Contributions

T. A. Assefa: Data curation (equal); Formal analysis (equal); Writing - original draft (equal); Writing - review & editing (equal). M. H. Seaberg: Data curation (equal); Formal analysis (equal); Investigation (equal); Writing - original draft (equal); Writing - review & editing (equal). A. H. Reid: Conceptualization (equal); Investigation (equal); Methodology (equal); Writing - review & editing (equal). L. Shen: Data curation (equal); Formal analysis (equal); Software (equal); Writing - review & editing (equal). V. Esposito: Formal analysis (equal); Software (equal); Writing - original draft (equal); Writing - review & editing (equal). G. L. Dakovski: Investigation (equal). W. Schlotter: Investigation (equal). B. Holladay: Software (equal). R. Streubel: Investigation (equal). S. A. Montoya: Conceptualization (equal); Investigation (equal); Methodology (equal). P. Hart: Methodology (equal). K. Nakahara: Methodology (equal). S. Moeller: Investigation (equal). S. D. Kevan: Supervision (equal). P. Fischer: Supervision (equal). E. E. Fullerton: Supervision (equal). W. Colocho: Methodology (equal). A. Lutman: Methodology (equal). F.-J. Decker: Methodology (equal). S. K. Sinha: Conceptualization (equal); Supervision (equal). S. Roy: Conceptualization (equal); Investigation (equal); Methodology (equal); Resources (equal); Supervision (equal). E. Blackburn: Funding acquisition (equal); Resources (equal); Supervision (equal); Writing - original draft (equal); Writing - review & editing (equal). J. J. Turner: Conceptualization (equal); Data curation (equal); Funding acquisition (equal); Investigation (equal); Methodology (equal); Project administration (equal); Resources (equal); Supervision (equal); Writing original draft (equal); Writing - review & editing (equal).

DATA AVAILABILITY

Raw data were generated at the LCLS large scale facility. Derived data supporting the findings of this study are available from the corresponding author upon reasonable request.

APPENDIX A: READOUT ELECTRONICS

This appendix describes the different maximum frame readout speeds used for the detector in the prototype instrument. This is also known as the analog-to-digital converter (ADC) speed or readout noise per electron. The table gives some examples of the maximum region of interest that can be measured for different repetition rates and readout noise rates of the detector. These can be chosen to match a given experiment based on the distribution of the scattering signal (Table I).

TABLE I. An example of different detector readout frame rates as a function of the active area in pixels for both ADC speeds of 3 and 1 MHz, the readout noise per electron. This running condition is only possible when the detector chip is blocked from the light outside the region of interest, as described in the main text. The ADC speed allows one to use the trade-off of readout noise vs readout speed.

Trigger rate (Hz)	3 MHz	1 MHz
120	90 × 90	50 × 50
60	155×155	85×85
30	255×255	140×140
10	470×470	275×275

APPENDIX B: TWO-PULSE SVD

By reconstructing two-pulse configurations to analyze the data, the constructed basis described in Sec. III B is no longer fully orthogonal, especially for shorter delays when the two pulses present a larger overlap. The vector representing the coefficients ξ in the two-pulse basis is found by solving the over-determined least-squares problem $\tilde{y} = W\xi$ for the waveform \tilde{y} . This can be solved numerically using the Moore–Penrose inverse of W,

$$W^{+} = (W^{*}W)^{-1}W^{*}, (B1)$$

to retrieve the value of ξ ,

$$\xi = W^{+} \tilde{y}, \tag{B2}$$

where the intensity of each pulse is given by taking the Euclidean norm of their respective coefficients. It should be noted that the pulse intensities are defined with respect to the basis constructed from the single-pulse data. Although the SVD on different sets of single-pulse waveforms generally provides very similar results, the total pulse amplitude distribution is optimally reconstructed when computed using the basis from single-pulses collected in the same run. This is important to keep in mind when averaging different datasets.

The reconstructed waveform is found by applying the projector WW^{\dagger} to the original waveform,

$$y = WW^{\dagger}\tilde{y},\tag{B3}$$

which is then used to fit the data with the two pulse amplitudes.

REFERENCES

¹R. Kubo, Rep. Prog. Phys. 29, 255 (1966).

² A. V. Chubukov, S. Sachdev, and J. Ye, Phys. Rev. B **49**, 11919 (1994).

M. S. Pierce, C. R. Buechler, L. B. Sorensen, J. J. Turner, S. D. Kevan, E. A. Jagla, J. M. Deutsch, T. Mai, O. Narayan, J. E. Davies, K. Liu, J. H. Dunn, K. M. Chesnel, J. B. Kortright, O. Hellwig, and E. E. Fullerton, Phys. Rev. Lett. 94, 017202 (2005).
 M. S. Pierce, J. E. Davies, J. J. Turner, K. Chesnel, E. E. Fullerton, J. Nam, R. Hailstone, S. D. Kevan, J. B. Kortright, K. Liu et al., Phys. Rev. B 87, 184428 (2013).
 X. Chen, C. Mazzoli, Y. Cao, V. Thampy, A. Barbour, W. Hu, M. Lu, T. Assefa, H. Miao, G. Fabbris, G. Gu, J. Tranquada, M. Dean, S. Wilkins, and I. Robinson, Nat. Commun. 10, 1435 (2019).

⁶Y. Shen, G. Fabbris, H. Miao, Y. Cao, D. Meyers, D. G. Mazzone, T. A. Assefa, X. M. Chen, K. Kisslinger, D. Prabhakaran, A. T. Boothroyd, J. M. Tranquada, W. Hu, A. M. Barbour, S. B. Wilkins, C. Mazzoli, I. K. Robinson, and M. P. M. Dean, Phys. Rev. Lett. 126, 177601 (2021).

- ⁷S. Brauer, G. Stephenson, M. Sutton, R. Brüning, E. Dufresne, S. Mochrie, G. Grübel, J. Als-Nielsen, and D. Abernathy, Phys. Rev. Lett. **74**, 2010 (1995).
- ⁸M. Sutton, S. G. J. Mochrie, T. Greytak, S. E. Nagler, L. E. Berman, G. A. Held, and G. B. Stephenson, Nature **352**, 608 (1991).
- ⁹F. Livet, F. Bley, R. Caudron, E. Geissler, D. Abernathy, C. Detlefs, G. Grübel, and M. Sutton, Phys. Rev. E **63**, 036108 (2001).
- ¹⁰K. Ludwig, F. Livet, F. Bley, J.-P. Simon, R. Caudron, D. Le Bolloc'h, and A. Moussaid, Phys. Rev. B 72, 144201 (2005).
- ¹¹S. K. Sinha, J. Phys.: Condens. Matter 13, 7511 (2001).
- ¹²G. Grübel, G. B. Stephenson, C. Gutt, H. Sinn, and T. Tschentscher, Nucl. Instrum. Methods Phys. Res., Sect. B 262, 357 (2007).
- ¹³O. G. Shpyrko, E. D. Isaacs, J. M. Logan, Y. Feng, G. Aeppli, R. Jaramillo, H. C. Kim, T. F. Rosenbaum, P. Zschack, M. Sprung, S. Narayanan, and A. R. Sandy, Nature 447, 68 (2007).
- ¹⁴C. S. Nelson, J. P. Hill, D. Gibbs, F. Yakhou, F. Livet, Y. Tomioka, T. Kimura, and Y. Tokura, Phys. Rev. B 66, 134412 (2002).
- ¹⁵J. J. Turner, K. J. Thomas, J. P. Hill, M. A. Pfeifer, K. Chesnel, Y. Tomioka, Y. Tokura, and S. D. Kevan, New J. Phys. **10**, 053023 (2008).
- ¹⁶S.-W. Chen, H. Guo, K. A. Seu, K. Dumesnil, S. Roy, and S. K. Sinha, Phys. Rev. Lett. 110, 217201 (2013).
- ¹⁷X. M. Chen, V. Thampy, C. Mazzoli, A. M. Barbour, H. Miao, G. D. Gu, Y. Cao, J. M. Tranquada, M. P. M. Dean, and S. B. Wilkins, Phys. Rev. Lett. 117, 167001 (2016).
- ¹⁸ K. A. Seu, S. Roy, J. J. Turner, S. Park, C. M. Falco, and S. D. Kevan, Phys. Rev. B 82, 012404 (2010).
- ¹⁹S. Sachdev and J. Ye, Phys. Rev. Lett. **69**, 2411 (1992).
- ²⁰M. Sikorski, Y. Feng, S. Song, D. Zhu, G. Carini, S. Herrmann, K. Nishimura, P. Hart, and A. Robert, J. Synchrotron Radiat. 23, 1171 (2016).
- ²¹L. J. Koerner, H. T. Philipp, M. S. Hromalik, M. W. Tate, and S. M. Gruner, J. Instrum. 4, P03001 (2009).
- ²²T. Kameshima, S. Ono, T. Kudo, K. Ozaki, Y. Kirihara, K. Kobayashi, Y. Inubushi, M. Yabashi, T. Horigome, A. Holland, K. Holland, D. Burt, H. Murao, and T. Hatsui, Rev. Sci. Instrum. 85, 033110 (2014).
- ²³ A. Allahgholi, J. Becker, A. Delfs, R. Dinapoli, P. Goettlicher, D. Greiffenberg, B. Henrich, H. Hirsemann, M. Kuhn, R. Klanner, A. Klyuev, H. Krueger, S. Lange, T. Laurus, A. Marras, D. Mezza, A. Mozzanica, M. Niemann, J. Poehlsen, J. Schwandt, I. Sheviakov, X. Shi, S. Smoljanin, L. Steffen, J. Sztuk-Dambietz, U. Trunk, Q. Xia, M. Zeribi, J. Zhang, M. Zimmer, B. Schmitt, and H. Graafsma, J. Synchrotron Radiat. 26, 74 (2019).
- ²⁴J. Stohr, Linac Coherent Light Source II (LCLS-II) Conceptual Design Report No. SLAC-R-978, 2011.
- ²⁵ W. Jo, F. Westermeier, R. Rysov, O. Leupold, F. Schulz, S. Tober, V. Markmann, M. Sprung, A. Ricci, T. Laurus, A. Aschkan, A. Klyuev, U. Trunk, H. Graafsma, G. Grübel, and W. Roseker, IUCrJ 8, 124 (2021).
- ²⁶C. Gutt, L.-M. Stadler, A. Duri, T. Autenrieth, O. Leupold, Y. Chushkin, and G. Grübel, Opt. Express 17, 55 (2009).
- ²⁷L. Shen, M. Seaberg, E. Blackburn, and J. J. Turner, MRS Adv. **6**, 221 (2021).
- ²⁸T. Osaka, M. Yabashi, Y. Sano, K. Tono, Y. Inubushi, T. Sato, S. Matsuyama, T. Ishikawa, and K. Yamauchi, Opt. Express **21**, 2823 (2013).
- ²⁹W. Roseker, S. O. Hruszkewycz, F. Lehmkühler, M. Walther, H. Schulte-Schrepping, S. Lee, T. Osaka, L. Strüder, R. Hartmann, M. Sikorski, S. Song, A. Robert, P. H. Fuoss, M. Sutton, G. B. Stephenson, and G. Grübel, Nat. Commun. 9, 1704 (2018).
- ³⁰ W. Lu, B. Friedrich, T. Noll, K. Zhou, J. Hallmann, G. Ansaldi, T. Roth, S. Serkez, G. Geloni, A. Madsen, and S. Eisebitt, Rev. Sci. Instrum. 89, 063121 (2018).
- ³¹Y. Sun, N. Wang, S. Song, P. Sun, M. Chollet, T. Sato, T. B. van Driel, S. Nelson, R. Plumley, J. Montana-Lopez, S. W. Teitelbaum, J. Haber, J. B. Hastings, A. Q. R. Baron, M. Sutton, P. H. Fuoss, A. Robert, and D. Zhu, Opt. Lett. 44, 2582 (2019).
 ³²M. H. Seaberg, B. Holladay, J. C. T. Lee, M. Sikorski, A. H. Reid, S. A. Montoya, G. L. Dakovski, J. D. Koralek, G. Coslovich, S. Moeller, W. F. Schlotter, R. Streubel, S. D. Kevan, P. Fischer, E. E. Fullerton, J. L. Turner, F.-J. Decker, S. K. Sinha, S. Roy, and J. J. Turner, Phys. Rev. Lett. 119, 067403 (2017).
- ³³Y. Sun, F.-J. Decker, J. Turner, S. Song, A. Robert, and D. Zhu, J. Synchrotron Radiat. 25, 642 (2018).

- ³⁴V. Esposito, X. Y. Zheng, M. H. Seaberg, S. A. Montoya, B. Holladay, A. H. Reid, R. Streubel, J. C. T. Lee, L. Shen, J. D. Koralek, G. Coslovich, P. Walter, S. Zohar, V. Thampy, M. F. Lin, P. Hart, K. Nakahara, P. Fischer, W. Colocho, A. Lutman, F.-J. Decker, S. K. Sinha, E. E. Fullerton, S. D. Kevan, S. Roy, M. Dunne, and J. J. Turner, Appl. Phys. Lett. 116, 181901 (2020).
- ³⁵ M. H. Seaberg, B. Holladay, S. A. Montoya, X. Y. Zheng, J. C. T. Lee, A. H. Reid, J. D. Koralek, L. Shen, V. Esposito, G. Coslovich, P. Walter, S. Zohar, V. Thampy, M. F. Lin, P. Hart, K. Nakahara, R. Streubel, S. D. Kevan, P. Fischer, W. Colocho, A. Lutman, F.-J. Decker, E. E. Fullerton, M. Dunne, S. Roy, S. K. Sinha, and J. J. Turner, Phys. Rev. Res. 3, 033249 (2021).
- ³⁶ N. G. Burdet, V. Esposito, M. H. Seaberg, C. H. Yoon, and J. J. Turner, Sci. Rep. 11, 19455 (2021).
- ³⁷Y. Sun, G. Carini, M. Chollet, F.-J. Decker, M. Dunne, P. Fuoss, S. O. Hruszkewycz, T. J. Lane, K. Nakahara, S. Nelson, A. Robert, T. Sato, S. Song, G. B. Stephenson, M. Sutton, T. B. Van Driel, C. Weninger, and D. Zhu, Phys. Rev. Lett. 127, 058001 (2021).
- ³⁸ A. A. Lutman, R. Coffee, Y. Ding, Z. Huang, J. Krzywinski, T. Maxwell, M. Messerschmidt, and H.-D. Nuhn, Phys. Rev. Lett. 110, 134801 (2013).
- 39 F.-J. Decker *et al.*, "Recent Developments and Plans for Two Bunch Operation with up to 1 μ s Separation at LCLS" FEL 2017, Santa Fe, TUP023.
- ⁴⁰ A. A. Lutman, T. J. Maxwell, J. P. MacArthur, M. W. Guetg, N. Berrah, R. N. Coffee, Y. Ding, Z. Huang, A. Marinelli, S. Moeller, and J. C. U. Zemella, Nat. Photonics 10, 745 (2016).
- ⁴¹ A. Marinelli, D. Ratner, A. Lutman, J. Turner, J. Welch, F.-J. Decker, H. Loos, C. Behrens, S. Gilevich, A. Miahnahri *et al.*, Nat. Commun. 6, 6369 (2015).
- ⁴²F.-J. Decker, K. L. Bane, W. Colocho, S. Gilevich, A. Marinelli, J. C. Sheppard, J. L. Turner, J. J. Turner, S. L. Vetter, A. Halavanau, C. Pellegrini, and A. A. Lutman, Sci. Rep. 12, 3253 (2022).
- ⁴³ P. Heimann, O. Krupin, W. F. Schlotter, J. Turner, J. Krzywinski, F. Sorgenfrei, M. Messerschmidt, D. Bernstein, J. Chalupský *et al.*, Rev. Sci. Instrum. **82**, 093104 (2011).
- ⁴⁴G. L. Dakovski, P. Heimann, M. Holmes, O. Krupin, M. P. Minitti, A. Mitra, S. Moeller, M. Rowen, W. F. Schlotter, and J. J. Turner, J. Synchrotron Radiat. **22**, 498 (2015).
- ⁴⁵P. Emma, R. Akre, J. Arthur, R. Bionta, C. Bostedt, J. Bozek, A. Brachmann, P. Bucksbaum, R. Coffee, F.-J. Decker *et al.*, Nat. Photonics 4, 641 (2010).
- ⁴⁶S. Droste, S. Zohar, L. Shen, V. E. White, E. Diaz-Jacobo, R. N. Coffee, A. H. Reid, F. Tavella, M. P. Minitti, J. J. Turner, J. S. Robinson, A. R. Fry, and G. Coslovich, Opt. Express 28, 23545 (2020).
- ⁴⁷ M. Beye, O. Krupin, G. Hays, A. H. Reid, D. Rupp, S. d. Jong, S. Lee, W.-S. Lee, Y.-D. Chuang, R. Coffee *et al.*, Appl. Phys. Lett. **100**, 121108 (2012).
- ⁴⁸O. Krupin, M. Trigo, W. F. Schlotter, M. Beye, F. Sorgenfrei, J. J. Turner, D. A. Reis, N. Gerken, S. Lee, W. S. Lee *et al.*, Opt. Express **20**, 11396 (2012).
- ⁴⁹R. Soufli, M. Fernández-Perea, S. L. Baker, J. C. Robinson, E. M. Gullikson, P. Heimann, V. V. Yashchuk, W. R. McKinney, W. F. Schlotter, and M. Rowen, Appl. Opt. 51, 2118 (2012).
- ⁵⁰J. Chalupský, P. Boháček, T. Burian, V. Hájková, S. P. Hau-Riege, P. A. Heimann, L. Juha, M. Messerschmidt, S. P. Moeller, B. Nagler, M. Rowen, W. F. Schlotter, M. L. Swiggers, J. J. Turner, and J. Krzywinski, Phys. Rev. Appl. 4, 014004 (2015).
- ⁵¹ V. Hájková, L. Juha, P. Boháček, T. Burian, J. Chalupský, L. Vyšín, J. Gaudin, P. A. Heimann, S. P. Hau-Riege, M. Jurek, D. Klinger, J. Pelka, R. Sobierajski, J. Krzywinski, M. Messerschmidt, S. P. Moeller, B. Nagler, M. Rowen, W. F. Schlotter, M. L. Swiggers, J. J. Turner, S. M. Vinko, T. Whitcher, J. Wark, M. Matuchová, S. Bajt, H. Chapman, T. Dzelzainis, D. Riley, J. Andreasson, J. Hajdu, B. Iwan, N. Timneanu, K. Saksl, R. Fäustlin, A. Singer, K. Tiedtke, S. Toleikis, I. Vartaniants, and H. Wabnitz, Proc. SPIE 8077, 807718 (2011).
- ⁵²J. Chalupsky, P. Bohacek, V. Hajkova, S. P. Hau-Riege, P. A. Heimann, L. Juha, J. Krzywinski, M. Messerschmidt, S. P. Moeller, B. Nagler *et al.*, Nucl. Instrum. Methods Phys. Res., Sect. A **631**, 130 (2011).
- ⁵³ K. Tiedtke, A. A. Sorokin, U. Jastrow, P. Juranić, S. Kreis, N. Gerken, M. Richter, U. Arp, Y. Feng, D. Nordlund *et al.*, Opt. Express **22**, 21214 (2014).
- ⁵⁴S. Moeller, G. Brown, G. Dakovski, B. Hill, M. Holmes, J. Loos, R. Maida, E. Paiser, W. Schlotter, J. J. Turner et al., J. Synchrotron Radiat. 22, 606 (2015).

- ⁵⁵D. Doering, Y.-D. Chuang, N. Andresen, K. Chow, D. Contarato, C. Cummings, E. Domning, J. Joseph, J. S. Pepper, B. Smith *et al.*, Rev. Sci. Instrum. **82**, 073303 (2011).
- ⁵⁶K. Kunnus, I. Rajkovic, S. Schreck, W. Quevedo, S. Eckert, M. Beye, E. Suljoti, C. Weniger, C. Kalus, S. Grübel *et al.*, Rev. Sci. Instrum. **83**, 123109 (2012).
- ⁵⁷S. Bernitt, G. V. Brown, J. K. Rudolph, R. Steinbrügge, A. Graf, M. Leutenegger, S. W. Epp, S. Eberle, K. Kubiček *et al.*, Nature **492**, 225 (2012).
- ⁵⁸T. Katayama, T. Anniyev, M. Beye, R. Coffee, M. Dell'Angela, A. Föhlisch, J. Gladh, S. Kaya, O. Krupin, A. Nilsson *et al.*, J. Electron Spectrosc. Relat. Phenom. **187**, 9 (2013).
- ⁵⁹ J. J. Turner, G. L. Dakovski, M. C. Hoffmann, H. Y. Hwang, A. Zarem, W. F. Schlotter, S. Moeller, M. P. Minitti, U. Staub, S. Johnson *et al.*, J. Synchrotron Radiat. **22**, 621 (2015).
- ⁶⁰ W. F. Schlotter, J. J. Turner, M. Rowen, P. Heimann, M. Holmes, O. Krupin, M. Messerschmidt, S. Moeller, J. Krzywinski, R. Soufli *et al.*, Rev. Sci. Instrum. **83**, 043107 (2012).
- ⁶¹ T. Osipov, C. Bostedt, J.-C. Castagna, K. R. Ferguson, M. Bucher, S. C. Montero, M. L. Swiggers, R. Obaid, D. Rolles, A. Rudenko, J. D. Bozek, and N. Berrah, Rev. Sci. Instrum. 89, 035112 (2018).
- ⁶² L. Strüder, S. Epp, D. Rolles, R. Hartmann, P. Holl, G. Lutz, H. Soltau, R. Eckart, C. Reich, K. Heinzinger *et al.*, Nucl. Instrum. Methods Phys. Res., Sect. A **614**, 483 (2010).
- ⁶³ D. L. Abernathy, G. Grübel, S. Brauer, I. McNulty, G. B. Stephenson, S. G. J. Mochrie, A. R. Sandy, N. Mulders, and M. Sutton, J. Synchrotron Radiat. 5, 37 (1998).
- ⁶⁴S. O. Hruszkewycz, M. Sutton, P. H. Fuoss, B. Adams, S. Rosenkranz, K. F. Ludwig et al., Phys. Rev. Lett. 109, 185502 (2012).
- ⁶⁵I. A. Vartanyants, A. Singer, A. P. Mancuso, O. M. Yefanov, A. Sakdinawat, Y. Liu, E. Bang, G. J. Williams, G. Cadenazzi, B. Abbey *et al.*, Phys. Rev. Lett. **107**, 144801 (2011).
- ⁶⁶J. J. Turner, J. Nelson, X. Huang, J. Steinbrener, and C. Jacobsen, Phys. Lett. A 377, 1150 (2013).
- ⁶⁷ J. C. T. Lee, J. J. Chess, S. A. Montoya, X. Shi, N. Tamura, S. K. Mishra, P. Fischer, B. J. McMorran, S. K. Sinha, E. E. Fullerton *et al.*, Appl. Phys. Lett. **109**, 022402 (2016).

- ⁶⁸ A. R. Sandy, L. B. Lurio, S. G. J. Mochrie, A. Malik, G. B. Stephenson, J. F. Pelletier, and M. Sutton, J. Synchrotron Radiat. 6, 1174 (1999).
- ⁶⁹ M. Schneider, C. M. Günther, B. Pfau, F. Capotondi, M. Manfredda, M. Zangrando, N. Mahne, L. Raimondi, E. Pedersoli, D. Naumenko, and S. Eisebitt, Nat. Commun. 9, 214 (2018).
- ⁷⁰Y. Liu, M. Seaberg, D. Zhu, J. Krzywinski, F. Seiboth, C. Hardin, D. Cocco, A. Aquila, B. Nagler, H. J. Lee, S. Boutet, Y. Feng, Y. Ding, G. Marcus, and A. Sakdinawat, Optica 5, 967 (2018).
- ⁷¹ X. Z. Yu, N. Kanazawa, Y. Onose, K. Kimoto, W. Z. Zhang, S. Ishiwata, Y. Matsui, and Y. Tokura, Nat. Mater. 10, 106 (2011).
- ⁷² X. Z. Yu, Y. Onose, N. Kanazawa, J. H. Park, J. H. Han, Y. Matsui, N. Nagaosa, and Y. Tokura, Nature 465, 901 (2010).
- ⁷³ F. Zheng, F. N. Rybakov, A. B. Borisov, D. Song, S. Wang, Z.-A. Li, H. Du, N. S. Kiselev, J. Caron, A. Kovács, M. Tian, Y. Zhang, S. Blügel, and R. E. Dunin-Borkowski, Nat. Nanotechnol. 13, 451 (2018).
- ⁷⁴F. Jonietz, S. Mühlbauer, C. Pfleiderer, A. Neubauer, W. Münzer, A. Bauer, T. Adams, R. Georgii, P. Böni, R. A. Duine *et al.*, Science **330**, 1648 (2010).
- ⁷⁵T. Nakajima, H. Oike, A. Kikkawa, E. P. Gilbert, N. Booth, K. Kakurai, Y. Taguchi, Y. Tokura, F. Kagawa, and T.-h. Arima, Sci. Adv. 3, e1602562 (2017).
- ⁷⁶Y. Tokunaga, X. Z. Yu, J. S. White, H. M. Rønnow, D. Morikawa, Y. Taguchi, and Y. Tokura, Nat. Commun. 6(1), 7638 (2015).
- ⁷⁷S. Heinze, K. Von Bergmann, M. Menzel, J. Brede, A. Kubetzka, R. Wiesendanger, G. Bihlmayer, and S. Blügel, Nat. Phys. 7, 713 (2011).
- ⁷⁸ M. C. Langner, S. Roy, S. K. Mishra, J. C. T. Lee, X. W. Shi, M. A. Hossain, Y.-D. Chuang, S. Seki, Y. Tokura, S. D. Kevan, and R. W. Schoenlein, *Phys. Rev. Lett.* **112**, 167202 (2014).
- ⁷⁹M. C. Langner, S. Roy, S. W. Huang, J. D. Koralek, Y.-D. Chuang, G. L. Dakovski, J. J. Turner, J. S. Robinson, R. N. Coffee, M. P. Minitti, S. Seki, Y. Tokura, and R. W. Schoenlein, Phys. Rev. Lett. 119, 107204 (2017).
- ⁸⁰R. Streubel, D. S. Bouma, F. Bruni, X. Chen, P. Ercius, J. Ciston, A. T. N'Diaye, S. Roy, S. D. Kevan, P. Fischer, and F. Hellman, Adv. Mater. 33, 2004830 (2021).
- ⁸¹ LCLS Data Analysis, Hit and peak finding algorithms, https://confluence.slac.stanford.edu/display/PSDM/Hit+and+Peak+Finding+Algorithms; last accessed January 06, 2022.